Acta Crystallographica Section B
Structural Science
ISSN 0108-7681

An experimental charge density of HEPES

Paweł Śledź,[a,b]‡ Radosław Kamiński,[a,c] Maksymilian Chruszcz,[b] Matthew D. Zimmerman,[b] Wladek Minor[b] and Krzysztof Woźniak[a]*

[a]Department of Chemistry, Warsaw University, Pasteura 1, 02-093 Warszawa, Poland, [b]Department of Molecular Physiology and Biological Physics, University of Virginia, 1340 Jefferson Park Avenue, Charlottesville, VA 22908, USA, and [c]Department of Chemistry, Warsaw University of Technology, Noakowskiego 3, 00-664 Warszawa, Poland

‡ Current address: Department of Chemistry, University of Cambridge, Lensfield Road, Cambridge CB2 1EW, England.

Correspondence e-mail: kwozniak@chem.uw.edu.pl

Received 1 March 2010
Accepted 15 June 2010

We report the experimental charge density of HEPES [4-(2-hydroxyethyl)-1-piperazineethanesulfonic acid], which is a common buffering agent. The structure was refined using the Hansen–Coppens formalism. The ability of the HEPES molecule to form stable intermolecular interactions and intermolecular hydrogen bonds in the crystal structure is discussed in terms of its buffering properties. The protonation mode observed in the crystal structure is different from that expected in solution, suggesting that additional factors must be taken into consideration in order to explain the solution properties of the compound. As ordered HEPES molecules are found in the active sites of proteins in several protein crystal structures, our results will allow for quantitative analysis of the electrostatic potential of the interacting surfaces of those proteins.

1. Introduction

The rapid development of molecular biology prompted the search for effective buffering agents, which resulted in the synthesis of a number of compounds that buffer effectively in the physiological pH range of 7.0–8.0. A set of 12 of them were described by Norman Good and co-workers in 1966 as suitable for biological applications and since then have been described as the 'Good' buffers. In addition to having buffering capacities near neutral pH, they were selected for other experimentally relevant properties like resistance to enzymatic degradation, lack of UV absorbance, lack of interference with biological assays and very limited cell-wall permeability. The Good buffers have been extensively tested in several model systems and are currently ubiquitous in biological research (Good *et al.*, 1966).

Several of the Good buffers are taurine-derived (or taurine-like) amphiphiles, which contain both a very strong acid (sulfonic acid) and a relatively weak base (amine), and are of particular interest for structural and mechanistic studies. The influence of the strong sulfonic acid on the amine tunes its basicity, allowing the compounds to be effective buffers at pH $\simeq$ 7.0. However, some of the analogous structures buffer effectively at higher pH values, and most noteworthy, their buffering properties may be significantly altered with slight changes to their chemical structure. Currently biologists have a large selection of different taurine-like buffers which buffer effectively at a wide range of pH values and are useful for many different applications, including crystallization of macromolecules. Table 1 summarizes the buffering properties of the most commonly used taurine-like buffers. Nonetheless, despite having been extensively studied, the electronic prop-

Table 1
Taurine-like organic buffers commonly used in biochemical studies.

Buffers marked by * are Good buffers.

Buffer	Effective pH range	Molecular structure
MES*	5.5–7.7	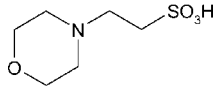
ACES*	6.1–7.5	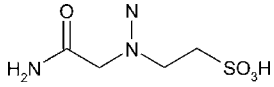
PIPES*	6.1–7.5	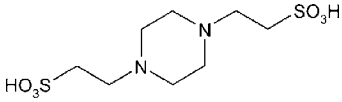
BES*	6.4–7.8	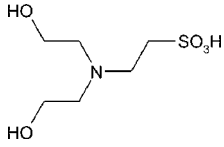
MOPS	6.5–7.9	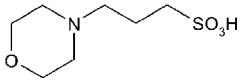
TES*	6.8–8.2	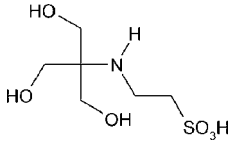
HEPES*	6.8–8.2	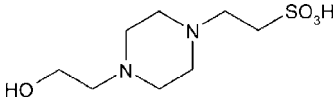
TAPS	7.7–9.1	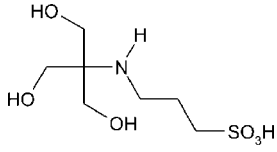
CHES	8.6–10.0	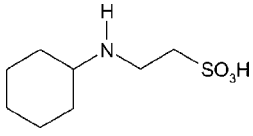
CAPS	9.7–11.1	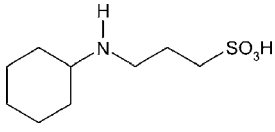

erties that influence the buffering capacities of taurine-like buffers have not been investigated by charge density studies.

1.1. The structure-buffering capacity relationship of taurine-like organic buffers

Trends in the buffering capacities of taurine-like compounds are apparent. When the taurine moiety is retained within the structure, simple substitutions at the N atom produce substances with buffering ranges varying from pH = 5.5 to 10.0. Further extensions of this range may be achieved by altering the length of the alkyl chain that separates the amine and the sulfonic group, as may be seen in MOPS, TAPS and CAPS (Table 1). The sulfonic group is usually very acidic with a pK_a of 1.0–3.0 and is usually deprotonated under physiological pH conditions, hence the group acts as a solubility enhancer. Good originally described the electron-withdrawing capacity of the substituents on the amine, the strain introduced by ring moieties (if present) and the order of the amine as the properties which were engineered to adjust the effective pH range of the taurine-like buffers (Good *et al.*, 1966).

Buffering compounds can now be studied in more detail using sophisticated instrumental approaches. In particular, interactions between acidic and basic moieties, the molecular geometry and the actual charge density distribution can be studied in the crystalline state using modern tools of X-ray crystallography. High-resolution experimental charge densities are especially valuable not only for rationalization of buffering properties, but mostly to better understand the interactions of these compounds with their binding sites on protein surfaces. Many taurine-like buffers are found in the crystal structures of several proteins, including the targets of structural genomics efforts. There have been recent examples of applications of high-resolution X-ray data to model electrostatic interactions of proteins with small molecules (Dominiak *et al.*, 2009; Fournier *et al.*, 2009). Using these techniques, it is possible to use experimental charge densities of buffers as probes to calculate detailed electrostatic properties of the binding sites and other 'hot spots' on protein surfaces.

1.2. HEPES as a model compound for taurine-like buffers

Crystal structures of several taurine-like buffers have been reported in the literature, including HEPES (Wouters *et al.*, 1996; Gao *et al.*, 2004; Śledź *et al.*, 2009), MES (Kubicki *et al.*, 2007), TAPSO (Wouters & Stalke, 1996) and MOPS (Chruszcz *et al.*, 2005). Examination of these data, as well as evaluation of preliminary crystallographic studies (data not shown), led

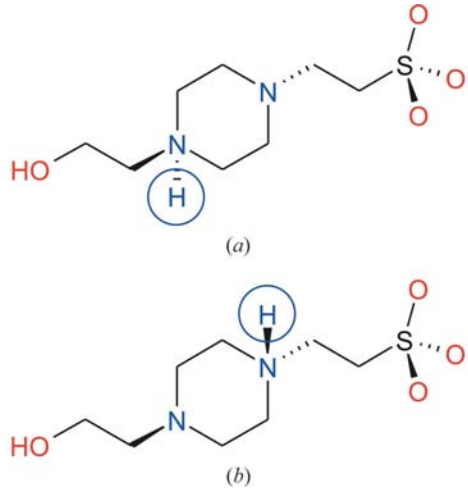

Figure 1
Protonation states of two polymorphs of HEPES: (*a*) crystallized from methanol and (*b*) from water.

Table 2
Crystal and X-ray diffraction data for HEPES.

Crystal data	
Chemical formula	$C_8H_{18}N_2O_4S$
M_r	238.31
Crystal system, space group	Orthorhombic, *Pbca*
Temperature (K)	100
a, b, c (Å)	8.3222 (2), 9.5441 (2), 27.0123 (6)
V (Å^3)	2145.53 (8)
Z	8
Radiation type	Mo $K\alpha$
$F(000)$	1024
μ (mm^{-1})	0.300
Crystal size (mm)	0.30 × 0.17 × 0.17
Data collection	
Diffractometer	Bruker Kappa APEXII Ultra
Absorption correction	Multi-scan (Blessing, 1995)
T_{min}, T_{max}	0.917, 0.960
No. of measured, independent and observed [$I > 2\sigma(I)$] reflections	183 825, 14 200, 9205
Completeness (%)	> 99
R_{int}	0.072
IAM refinement	
No. reflections/restraints/parameters	14 200/0/144
GoF	1.046
R_1/wR_2 [for $I > 2\sigma(I)$]	0.035/0.090
R_1/wR_2 (for all data)	0.070/0.105
$\Delta\rho_{max}$, $\Delta\rho_{min}$ (e Å^{-3})	0.647, −0.819
Multipole refinement	
No. of reflections [for $I > 3\sigma(I)$]/parameters	7812/677 = 11.54
R_1/wR_1 [for $I > 3\sigma(I)$]	0.023/0.026
R_2/wR_2 [for $I > 3\sigma(I)$]	0.027/0.048
GoF [for $I > 3\sigma(I)$]	1.171
$\Delta\rho_{max}$, $\Delta\rho_{min}$ (e Å^{-3})	0.250, −0.305

Computer programs used: *APEX*2 software, *SAINT* (Bruker AXS, 2008), *SORTAV* (Blessing, 1987, 1989, 1995), *SHELXS*97 (Sheldrick, 2008), *XD*2006 (Volkov *et al.*, 2006).

us to choose HEPES as the most promising model compound for very high-resolution X-ray diffraction experiments. Crystals of HEPES, initially obtained by slow evaporation of a water solution, exhibited an ordered structure with only one molecule in the asymmetric part of the unit cell, making it suitable for X-ray charge density studies (Śledź *et al.*, 2009). HEPES buffers effectively at pH 6.8–8.2, with its effective pK_a very close to the physiological pH range, making it one of the most widely applied buffers in biological research. The HEPES molecule has two amine N atoms in the ring, placed in different chemical environments – one uses SO_3H as an electron-withdrawing group (EWG), and the second one is linked to a hydroxyl group, placed analogously. Thus, this chemical structure can model the effects of two different EWGs within a single charge density distribution and moreover can be used to analyze strain effects created by a ring structure. Moreover, HEPES may be considered a taurine-derived buffer. While the experimental charge density for taurine has been determined (Hibbs *et al.*, 2003), the taurine charge density does not cover all of the possible interactions that HEPES can form.

Hundreds of macromolecular crystal structures with HEPES have been made publicly available in the Protein Data Bank to date, most of them low-resolution protein structures with ordered HEPES molecules bound to the macromolecule (255 as of December 2009). Work on the elucidation of the role of HEPES in protein crystallization, its ability to interact with a putative enzyme binding site, and its relationship with known or possible protein binders is currently under way and will be reported elsewhere. Two small molecule crystal structures of HEPES with two different supramolecular arrangements have been solved up to date – one crystallized from methanol [Wouters *et al.*, 1996; referred to from now on as HEPES(MeOH)], and one from water [Gao *et al.*, 2004; Śledź *et al.*, 2009, referred to from now on as HEPES(H_2O)]. These two polymorphs do not contain molecules of solvents. Significant differences in the HEPES molecule itself are observed in the protonation pattern (Fig. 1). In both cases a hydrogen bond is present between the protonated amine and the sulfonic acid anion, yet different N atoms are protonated. Both crystal forms HEPES(MeOH) and HEPES(H_2O) exhibited two distinct hydrogen bonds: $SO_3\cdots H-N$ and $O-H\cdots N$.

In this paper we discuss the influence of geometric and electronic factors on buffering properties and possible interactions made by HEPES using high-resolution X-ray diffraction experiments.

2. Experimental

2.1. Crystals

Crystals of HEPES(H_2O) were obtained from Aldrich (H3375-25G). No further crystallization was needed, as single crystals suitable for high-resolution X-ray diffraction experiment were present in the lot No. 038K5406.

2.2. Data collection

Single-crystal X-ray high-resolution measurement of HEPES(H_2O) was performed on a Bruker Kappa APEX II Ultra diffractometer equipped with a TXS rotating anode (Mo $K\alpha$ radiation, λ = 0.71073 Å), multi-layer optics and an Oxford Cryosystems nitrogen gas-flow apparatus. A single crystal of suitable size was attached to a cactus spine using *Paratone N* oil, mounted on a goniometer head 50 mm from the APEX II CCD camera and maintained at a temperature of 100 K. Details of the data collection are given in Table 2. The data collection strategy was optimized and monitored using the appropriate algorithms implemented by the *APEX*2 program (Bruker AXS, 2008). Only the ω scans were taken into account, using 0.5° intervals with a counting time of 5, 10, 20, 40 or 60 s (dependent on the resolution range), resulting in a total of 5670 frames. Determination of the unit cell parameters and integration of the raw images were performed with the *APEX*2 suite of programs (integration was done by *SAINT*; Bruker AXS, 2008). The dataset was corrected for Lorentz and polarization effects. The multi-scan absorption correction, scaling and merging of reflections were carried out with *SORTAV* (Blessing, 1987, 1989, 1995).

2.3. IAM refinement

The structure was solved by direct methods using *SHELXS*97 (Sheldrick, 2008) and refined using *SHELXL*97 (Sheldrick, 2008) using the IAM approximation. The refinement was based on F^2 for all reflections except those with very negative F^2. Weighted R factors (wR) and all goodness-of-fit (S) values are based on F^2. Conventional R factors are based on F with F set to zero for negative F^2. The $F_o^2 > 2\sigma(F_o^2)$ criterion was used only for calculating R factors and is not relevant to the choice of reflections for the refinement. The R factors based on F^2 are about twice as large as those based on F. Scattering factors were taken from the *International Tables for Crystallography* (2006). All non-H atoms were refined anisotropically. H atoms of C—H bonds were placed in idealized positions, those from O—H and N—H bonds were refined isotropically (these H atoms were visible on difference-density maps). The lattice parameters, including the final R indices obtained by spherical refinement, are presented in Table 2.

2.4. Multipole refinements

Multipole refinement of HEPES(H_2O) was performed using the XDLSM module of the *XD*2006 program suite (Volkov *et al.*, 2006), using the Hansen–Coppens formalism (Hansen & Coppens, 1978). In this formalism, the total atomic electron density (of the kth atom) is a sum of three components

$$\rho_k(\mathbf{r}) = \rho_{kc}(\mathbf{r}) + P_{kv}\kappa_k^3\rho_{kv}(\kappa\mathbf{r}) + \sum_{l=0}^{l_{\max}}\sum_{m=-l}^{l} P_{klm}\kappa_{kl}'^3 R_{kl}(\kappa_{kl}'\mathbf{r})d_{klm}(\theta,\varphi), \quad (1)$$

where ρ_{kc} and ρ_{kv} are spherical core and valence densities, respectively. The third term contains the sum of the angular functions (d_{klm}) that take into account aspherical deformations. The angular functions d_{klm} are real spherical harmonic functions, which are normalized for the electron density. The coefficients P_{kv} and P_{klm} are multipole populations for the valence and deformation density multipoles, respectively. κ and κ' are scaling parameters which control the expansion or contraction of the valence and deformation densities, respectively. In the Hansen–Coppens formalism, P_{kv}, P_{klm}, κ and κ' are refinable parameters together with the atomic coordinates and thermal motion coefficients. Here the P_{k00} parameter was not refined as it is highly correlated with P_{kv}.

The least-squares multipole refinement was based on F^2, and included only those reflections having $I > 3\sigma(I)$ and resolution up to 1.1 Å^{-1}. Atomic coordinates x, y and z and anisotropic displacement parameters (U^{ij}) for each atom were taken from the spherical refinement and freely refined. Each atom was assigned core and spherical-valence scattering factors derived from Su and Coppens wavefunctions (Su & Coppens, 1998). A single-ζ Slater-type radial function multiplied by density-normalized spherical harmonics was used to describe the valence deformation terms. For this model the standard (4,4,4,4,4) setting of the sulfur atomic scattering factor was used ($\zeta = 7.2778$ Å^{-1}). The multipole expansion was truncated at the hexadecapole ($l_{\max} = 4$) and quadrupole ($l_{\max} = 2$) levels for all non-H and H atoms. The valence-deformation radial fits were described by the use of their expansion–contraction parameters κ and κ', of which only κ was refined for non-H atoms. Identical values of the κ' parameter was used for all $l > 0$ multipoles for all other non-H atoms and kept unrefined at values of 1.00 and 1.20 for non-H and H atoms, respectively. No symmetry constraints were applied. The parameters refined at each stage of the refinement strategy were as follows:

(i) only the scale factor (which was also refined in all other stages);

(ii) the coordinates together with displacement parameters for non-H atoms with high-angle data ($\sin\theta/\lambda > 0.8$ Å^{-1});

(iii) coordinates together with isotropic displacement parameters for H atoms with low-angle data ($\sin\theta/\lambda < 0.6$ Å^{-1});

(iv) the H-atom positions (which were shifted along bond directions to standardized average neutron values: 0.967, 1.009 and 1.092 Å for O—H, N—H and C—H bond distances, respectively; Allen *et al.*, 1987) and the displacement parameters for non-H atoms at high-angle data ($\sin\theta/\lambda > 0.6$ Å^{-1});

(v) estimation of anisotropic displacement parameters for H atoms, using the SHADE server (Madsen, 2006 – such a procedure has been recently shown to be the best approach, at least within the Hansen–Coppens approximation, for H-atom treatment – Hoser *et al.*, 2009);

(vi) multipole parameters refined in a stepwise manner;

(vii) coordinates and displacement parameters together with all multipole populations;

(viii) coordinates and displacement parameters together with all multipole populations and κ parameters.

Proper deconvolution of thermal motion from the density features was tested by the Hirshfeld rigid-bond test (Hirshfeld, 1976). None of the differences of mean-squares displacement amplitudes (DMSDA) were higher than the upper limit (0.001 Å^2) – the highest value was equal to 8×10^{-4} Å^2 for the S1—C1 bond (which was the bond with the biggest difference in atomic masses).

According to the above general refinement strategy, several models with different scattering factors were tested but there were no significant changes. The maximum and minimum of residual density were equal to + 0.250 and −0.305 e Å^{-3}. The residual-density maps show some smaller randomly distributed deviations, but mostly near the S atom. The deformation density maps also show some deviations within this region (with a small maximum at the S atom), which could not be improved by any model. It has to be noted that similar problems with the S atom description were pointed out by Hibbs and co-workers in taurine refinement (Hibbs *et al.*, 2003), and so far no obvious solution has been found. The scattering factors proposed by Dominiak & Coppens (2006) also did not improve any of the above models. The presence of anharmonic vibrations was also excluded, as their refinement did not improve the model. One of the possible explanations is

the electron-withdrawing effect of O atoms bound to the S atom.

For details (statistical descriptors characterizing the refinement, list of highest residual-density peaks and troughs, residual-density and deformation maps *etc.*) see Table 2 and the supplementary materials[1].

2.5. Theoretical calculations

Single point calculations both with and without the presence of the electric field were carried out with the *GAUSSIAN*03 suite of programs (Frisch *et al.*, 2004) using the Hartree–Fock method with a 6-31G** basis set (Petersson *et al.*, 1988). The geometry was taken from the final step of the multipole refinement. The averaged electric field was calculated with the program *LORENTZ* (see *Acknowledgements*). The whole dipole moment calculation was carried out iteratively, as proposed by Spackman and co-workers (Spackman *et al.*, 2007), and converged after 5 cycles. The aug-cc-pVDZ (Woon & Dunning, 1993) with Becke-style three-parameter density-functional method using the Lee–Yang–Parr correlation functional – B3LYP (Becke, 1993; Lee *et al.*, 1988) was also tested, but did not lead to significantly different results, as the model to calculate the electric field is still very simple.

2.6. Topological analysis of the electron density

The experimental charge-density distributions obtained by a multipolar approach were analysed with the XDPROP and TOPXD modules of the *XD*2006 suite. Using Bader's Quantum-Theory-Atoms-in-Molecules (QTAIM; Bader, 1990) the bond-critical points (BCPs), ring-critical points (RCPs) and cage-critical points (CCPs) of the electron-density distribution were found. Also, the Laplacian of the electron density was analyzed in the same way, yielding (for example) the positions and parameters of valence-shell charge concentrations (VSCCs). Finally, the integrated properties over atomic basins (Ω), such as atomic charges or atomic dipole moments, were calculated according to the given formulae (for the kth atom)

$$Q_k(\Omega_k) = Z_k - \int_{\Omega_k} \rho(\boldsymbol{r})\mathrm{d}\boldsymbol{r} \quad \text{and} \quad \mu_k(\Omega_k) = \int_{\Omega_k} \rho(\boldsymbol{r})\boldsymbol{r}\mathrm{d}\boldsymbol{r}. \quad (2)$$

3. Results and discussion

3.1. Structural X-ray analysis

Before attempting crystallization optimization we found that many commercially available batches of HEPES contain crystals suitable for diffraction measurements (Fig. 2). Thus, a commercially available crystal was subjected to X-ray diffraction analysis, and the structure was solved and refined using an Independent Atom Model (IAM). A structure similar to the previously described structure of HEPES(H_2O) (Gao *et al.*, 2004) crystallized from water was found. In our data a residual electron density for a H atom forming a N—H···O hydrogen bond was found near the N1 atom. The placement of this hydrogen on nitrogen is temperature independent, as the measurements were taken both at 100 and 293 K, as briefly discussed previously (Śledź *et al.*, 2009). The supporting structural analysis included here is based on the final multipolar model.

The labeling scheme of the HEPES atoms is shown in Fig. 3 and selected geometrical parameters are presented in Table 3. HEPES(H_2O) crystallizes in the orthorhombic *Pbca* space group with one molecule in the asymmetric unit of the unit cell. No atoms occupy any special positions. The piperazine ring of the molecule exists in a low-energy chair conformation with the substituents at N atoms in equatorial positions. As the H1 atom is located bound to the N1 atom, the geometry of the bonds near the two N atoms in the HEPES molecule differ. Specifically, the C—N1 bond lengths are slightly longer (by *ca* 0.02–0.03 Å) than the corresponding C—N2 bonds. Also, the corresponding C—N—C bond angles differ by about 1°, resulting in a more significantly pyramidal structure about the N1 atom. This effect is the outcome of the protonation of the atom, confirming the assignment of the proton to the position. A similar effect was also observed when the previously published structure of HEPES(H_2O) (Gao *et al.*, 2004) was inspected. Furthermore, crystals of HEPES(H_2O) published by Gao and co-workers were reported to be green, while HEPES(H_2O) is a white powder and forms crystals which are colorless. The green color might have been due to accumulation of impurities, as the crystallization experiment was carried out for a very long time.

To find out whether the different location of the proton is due either to the effect of restraints applied to the previously published data (Gao *et al.*, 2004) or impurities within the crystal, we re-refined the published structure of HEPES(H_2O) against the structure factors deposited by Gao *et al.* using the IAM model without additional restraints. This resulted in a similar protonation pattern as was seen in our crystals, with no

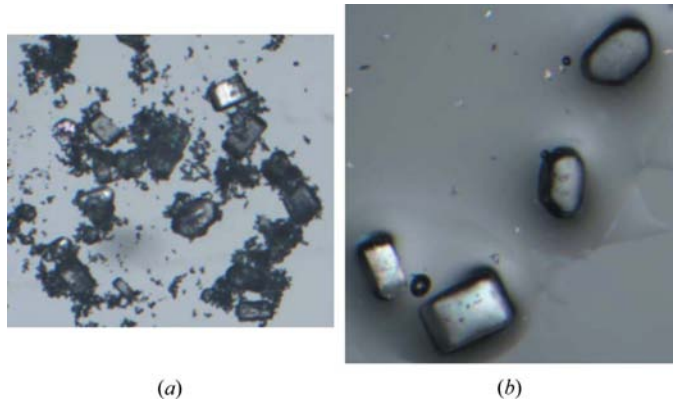

Figure 2
Crystals of HEPES: (*a*) taken straight from the commercial preparation; (*b*) washed and covered with oil just prior to mounting on the goniometer head.

[1] Supplementary data for this paper are available from the IUCr electronic archives (Reference: PI5006). Services for accessing these data are described at the back of the journal.

Table 3
Selected geometrical parameters for the HEPES structure.

S1—O1	1.4729 (4)	N1—C4	1.4922 (6)
S1—O2	1.4491 (5)	N2—C5	1.4679 (6)
S1—O3	1.4497 (6)	N2—C6	1.4691 (6)
S1—C1	1.7833 (4)	N2—C7	1.4694 (6)
N1—C2	1.4977 (6)	O4—C8	1.4164 (7)
N1—C3	1.4939 (6)		
C2—N1—C3	110.88 (4)	C5—N2—C6	108.36 (3)
C2—N1—C4	113.13 (4)	C5—N2—C7	112.29 (3)
C3—N1—C4	109.52 (3)	C6—N2—C7	108.82 (4)
O1—S1—C1—C2	−59.7 (1)	N2—C7—C8—O4	−76.0 (1)
S1—C1—C2—N1	−159.1 (1)		

Table 4
Geometry of weak inter- and intramolecular interactions.

	D—H (Å)	H···A (Å)	D···A (Å)	D—H···A (°)
N1—H1···O1^{i}	1.009	1.739	2.7364 (6)	169.1
C1—H1B···O1^{i}	1.092	2.467	3.3081 (6)	132.9
O4—H2···N2^{ii}	0.967	1.870	2.8309 (6)	172.1
C1—H1A···O2^{iii}	1.092	2.521	3.3898 (7)	135.7
C4—H4B···O2^{iii}	1.092	2.429	3.0761 (6)	116.5
C4—H4A···O3^{iv}	1.092	2.432	3.1887 (8)	125.2
C6—H6B···O3^{iv}	1.092	2.557	3.0936 (7)	109.2
C5—H5B···O4	1.092	2.350	3.0475 (6)	120.1

Symmetry codes: (i) $x+\frac{1}{2}, -y+\frac{1}{2}, -z+2$; (ii) $x+\frac{1}{2}, y, -z+\frac{3}{2}$; (iii) $x-\frac{1}{2}, -y+\frac{1}{2}, -z+2$; (iv) $-x+1, -y+1, -z+2$.

electron density, indicating the H atom bound to the O atom. Note that the same perturbation of the six-membered ring geometry (elongation of nitrogen–carbon bonds near the protonated N atom) was observed in our structure as well as in previously published structures of HEPES(H_2O) (Gao *et al.*, 2004; Śledź *et al.*, 2009). As one of the O atoms – namely O1 – is engaged in hydrogen bonding, the S1—O1 bond length is significantly longer than the remaining ones. Moreover, all other bond lengths are within common ranges for organic compounds and all torsion angles adopt synclinal or antiperiplanar low-energy conformations. An additional weak interaction is present within the molecule to stabilize this conformation – namely the weak C5—H5B···O4 interaction (Table 4).

In different polymorphs different N atoms are protonated. As a consequence, different intermolecular structures are formed. The geometries of the weak interactions for HEPES(H_2O) are shown in Table 4. As previously suggested, a possible difference in the hydrogen-bonding pattern might originate from the difference in the pK_a parameters of the amine moieties. In the case of the structure obtained from water, the conformation of the $-CH_2-CH_2-SO_3$ moiety is different compared with HEPES(MeOH), thus more or less flat hydrogen-bonded layers perpendicular to the Y direction are formed (Fig. 4*a*) rather than a three-dimensional network. Such layered structures are connected by weak C—H···O interactions. Interestingly, the geometry of the strong O—H···N hydrogen bond is very similar in both structures. The reason why different polymorphs are obtained from water

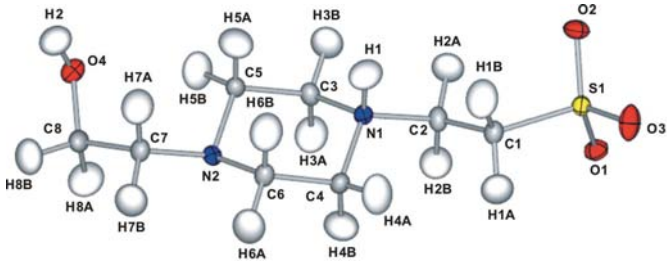

Figure 3
Labeling of atom representations and estimation of atomic displacement motions as ADPs after final multipole refinement. Ellipsoids are drawn at the 70% probability level.

versus methanol is still unknown. One possibility is that the two solvents stabilize different conformations just before building the crystal lattice. When crystals from the same batch used in diffraction experiments were dissolved in deionized water to a concentration of 50 mM, its measured pH was 5.30. This corresponds to a situation where the acidity of the sulfonic group was partially compensated for by the amines, so one should expect the predominant HEPES species to be zwitterion with one of the amines protonated. Such a situation is observed in the crystal structure of HEPES(H_2O), corresponding to this prediction. To address the issue of different protonation states, we have also attempted to crystallize HEPES after adjusting the pH of the saturated solution to different values, yet no diffraction quality crystals were obtained.

A very convenient way of analyzing intermolecular interactions is the use of a Hirshfeld surface (Spackman & Byrom,

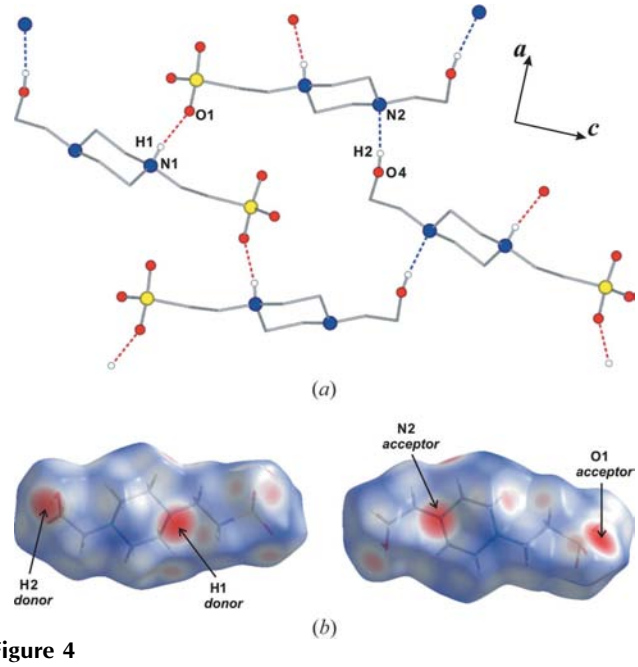

Figure 4
(*a*) Structural moiety present in hydrogen-bonded layers, as viewed along the Y axis; (*b*) Hirshfeld surfaces mapped with the d_{norm} property, showing the donor and acceptor atoms from strong hydrogen bonds. The red color indicates that the atom distances are smaller than the sum of the van der Waals radii.

1997; Spackman & Jayatilaka, 2009), which is defined as the surface where the ratio of electron densities of the promolecule and procrystal is equal to 0.5. A number of different properties may be mapped on such a surface, such as d_i (the distance from a point on the surface to the nearest nucleus *inside* the surface), d_e (the distance from a point on the surface to the nearest nucleus *outside* the surface) and d_{norm} (the normalized contact distance). The Hirshfeld surface of HEPES mapped with d_{norm} clearly shows where the donors and acceptors of strong hydrogen bonds are located (the red color indicates a high value of d_{norm} on the surface where the distance is shorter than the sum of the van der Waals radii; Fig. 4*b*). Also, the surface is covered with places where other weaker intermolecular interactions are present. In order to check whether other C—H···O interactions play an important role, a so-called 'fingerprint' plot (defined as a plot of d_i *versus* d_e) is presented in Fig. 5. Most of the interactions are non-bonding H···H contacts (covering 49.9% of the surface). The other main interactions are H···O (21.5%) and O···H (25.4%) contacts, covering almost all of the remaining surface responsible for the N—H···O and C—H···O hydrogen bonds.

Table 5
Selected topological parameters [$\rho(\mathbf{r}_{BCP})$ and $L(\mathbf{r}_{BCP})$ the negative Laplacian values] at BCPs for HEPES.

Bond	$\rho(\mathbf{r}_{BCP})$ (e Å^{-3})	$L(\mathbf{r}_{BCP})$ (e Å^{-5})
S1—O1	2.41 (4)	22.4 (2)
S1—O2	2.47 (4)	20.4 (2)
S1—O3	2.29 (4)	6.6 (2)
S1—C1	1.44 (3)	7.10 (8)
O4—C8	1.87 (5)	17.2 (2)
N1—C2	1.71 (4)	11.6 (2)
N1—C3	1.74 (4)	10.4 (2)
N1—C4	1.71 (4)	12.5 (2)
N2—C5	1.88 (4)	13.1 (1)
N2—C6	1.86 (4)	11.8 (2)
N2—C7	1.86 (4)	13.5 (2)
C1—C2	1.70 (4)	11.1 (1)
C7—C8	1.79 (4)	13.7 (1)
N1—H1	2.36 (8)	41.8 (6)
O4—H2	2.43 (8)	49.6 (7)

The strong N···H interactions unexpectedly cover a relatively small part of the interaction space, apparently being quite directional. The same is true for the N—H···O interactions, but they are not visible on the 'fingerprint' because of the domination of a large number of C—H···O weak interactions.

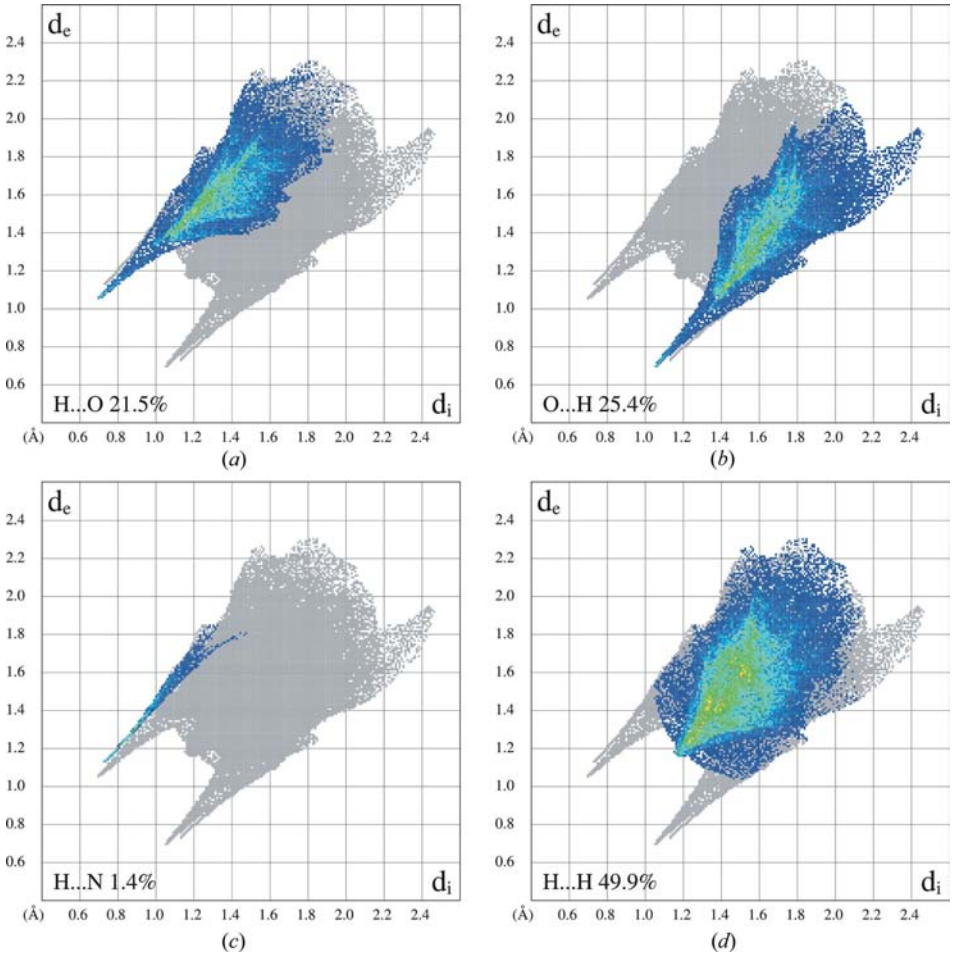

Figure 5
Decomposition of the Hirshfeld 'fingerprint' plot for the HEPES molecule, showing the areas of the surface containing different types of contacts: (*a*) H···O contacts (21.5%); (*b*) O···H contacts (25.4%); (*c*) H···N contacts (1.4%); (*d*) H···H contacts (49.9%).

3.2. Experimental charge-density studies of HEPES(H_2O)

In order to gain insight into the electronic properties of HEPES, we analyzed high-resolution X-ray data using the Hansen–Coppens model for a data set collected at 100 K using QTAIM.

3.2.1. BCP properties. The molecular graph is presented in Fig. 6. All predicted BCPs which correspond to the covalent bonds were found (see Table 5 for numerical parameters of BCPs) as well as additional ones for the weak intermolecular C—H···O interaction. In all cases, the values of the electron density and its Laplacian are within normal ranges for such types of organic compounds. For the S—O bonds, the value of the electron density is slightly higher than 2.0 e Å^{-3}, as the S atom has more electrons and quite high polarizability. Also, in the case of the donating N1—H1 and O4—H2 bonds, the values of electron density are relatively high, which

Table 6
AIM charges for selected atoms in HEPES.

Atom	Q (e)
S1	+2.437
O1	−1.258
O2	−1.265
O3	−1.211
O4	−1.030
N1	−0.968
N2	−0.882
H1	+0.500
H2	+0.626

is due to the short distances between the BCPs and H-atom nuclei. Considering the Laplacian, the highest values are observed for the S1—C1 and N1—C2 bonds, which are due to the fact that these bonds are longer than can be expected. Interestingly, there is a significant difference between the Laplacian and electron-density values for the S1—O3 bond in comparison to the S1—O1 and S1—O2 bonds, which cannot be explained by conformational or crystal packing effects. Also, the O1 is involved in a strong hydrogen bond. The presence of a hydrogen bond increases the bond length and thus the BCP shifts away from the S atom by *ca* 0.02 Å.

In the case of the C5—H5*B*···O4 contact, it was impossible to find the BCP and consequently the interaction line. This comes from the fact that the electron density is very flat in this region, indicating a minor structural instability. However, such an insignificant interaction should be present here owing to the proximity of the atoms in space and the overall conformation of the side chain.

3.2.2. Electrostatic properties. The electrostatic potential (ESP) mapped on an electron-density isosurface (see Fig. 7) gives a very valuable qualitative description of possible electrostatic interactions around the molecule. The sulfonic group possesses a very negative ESP while most of the rest of the molecule is positive, in fact the only other atom that exhibits a negative ESP value is O4. This suggests that such a distinct feature would be a handle for HEPES molecular recognition and stands in accordance with our preliminary observation of HEPES interacting with macromolecules mainly through sulfonic group electrostatic interactions.

The dipole moment obtained experimentally from the multipole populations is equal to 34.86 D. This quite high value comes from a strong polarization of the whole molecule. This result was compared to a value calculated by the theoretical model of Spackman and co-workers (Fig. 8; Spackman *et al.*, 2007). By using this method it was possible to estimate the dipole moment in the crystalline state, taking into account the averaged electric field from neighboring heavy atoms. The calculated dipole moment is equal to 24.00 D, which is a small enhancement in comparison to that of the isolated molecule (22.81 D). We believe that such a significant discrepancy between theory and experimental results from the simplified theoretical model or experimental errors or both. Also, it has recently been shown that the dipole moment is very sensitive even to the choice of multipole model (Bąk *et al.*, 2009, and references therein). Many examples of dipole moment analysis are present for different types of zwitterionic molecules. One of the most recent example of OVHIS molecule (Drašković *et al.*, 2010) deals with enormous dipole moment enhancement while comparing the experimental value (42.4 D) with the calculated one (25.5 D). This work and similarly our findings contribute to the list of cases where theoretical and experimental values differ very significantly, in disagreement with the conclusions drawn by Spackman (1992). Nevertheless, experimental and theoretical dipole moments have the same direction with only 5.8° of difference, showing that despite discrepancies in value the direction was reliably determined (Fig. 8).

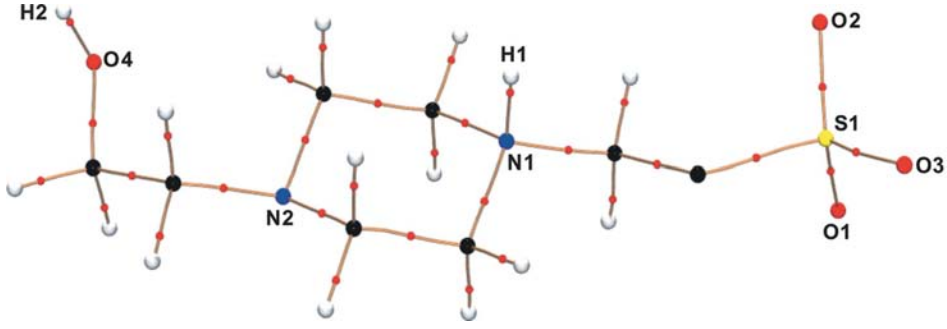

Figure 6
Molecular graph with atoms, critical points and bond paths of the HEPES molecule in the crystal (large red spheres – O atoms, large yellow sphere – S atom, large blue spheres – N atoms, large black spheres – C atoms, large white spheres – H atoms, small red spheres – BCPs, lines – BPs).

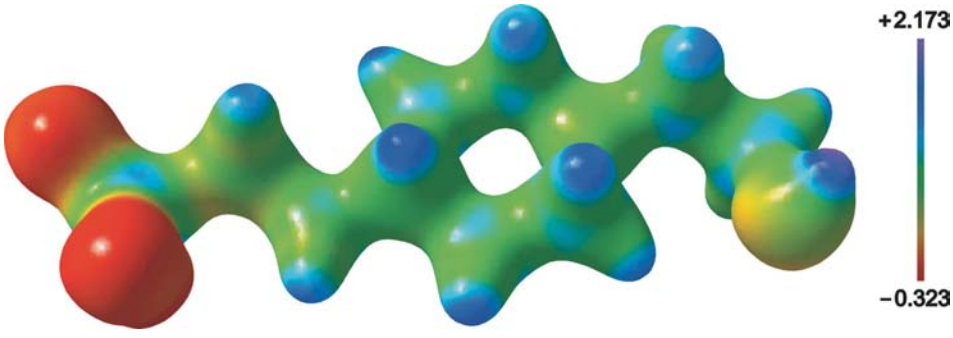

Figure 7
Isosurface of electron density with mapped electrostatic potential, contoured at a $\rho(\boldsymbol{r})$ value of 0.65 e Å^{-3}.

3.2.3. Properties of N and S atoms. The electronic properties

Table 7
Numerical parameters of the VSCCs around the N1, N2 and S1 atoms.

The notation $\rightarrow X$ denotes the direction of the CCs to atom X; LP_Y denotes the respective electron lone pair at atom Y.

Atom	Direction	$L(\boldsymbol{r})$ (e Å^{-5})
N1	$\rightarrow$ H1	85.9
	$\rightarrow$ C2	68.3
	$\rightarrow$ C3	61.0
	$\rightarrow$ C4	73.0
N2	LP_{N2}	79.6
	$\rightarrow$ C5	53.4
	$\rightarrow$ C6	57.0
	$\rightarrow$ C7	62.1
S1	$\rightarrow$ O1	22.4
	$\rightarrow$ O2	20.7
	$\rightarrow$ O3	12.8
	$\rightarrow$ C1	26.6

of two chemically distinct N atoms differ quite significantly. Table 6 shows the integrated AIM charges calculated according to Bader's theory. Both N atoms possess negative charges, but N2 seems to be less negative (by *ca* −0.04 e) than N1. For N1 the dipole moment magnitude is 0.128 D, while for N2 it is 0.298 D. These dipole moments are directed either to the H1 atom or to the lone pair. Significant differences between these two N atoms became clear when the Laplacian distribution was analyzed. Four VSCCs were found (see Table 7) around each N atom. In the case of N1, all of them are denoted as bonding CCs (charge concentrations), owing to their directions towards the closest bonded atoms (Fig. 9*a*). In the case of N2, one non-bonding VSCC is found, corresponding to the lone electron pair at this atom. Analysis of numerical parameters at these (3,−3) critical points of the negative Laplacian [$L(\boldsymbol{r})$] distribution shows that the most prominent VSCCs are directed towards the H atom (*ca* 86 e Å^{-5}) and lone electron pair (*ca* 80 e Å^{-5}) for the N1 and N2 atoms (Fig. 9*b*).

For the S atom four bonding VSCCs are found, directed toward O and C atoms. As the S atom has one shell more than the other atoms of the molecule such as carbon, the VSCCs are less pronounced and their values are much lower. The values of the negative Laplacian at (3,−3) critical points differ for the O1, O2 and O3 atoms. The CCs directed to the O1 atom is the most pronounced one (*ca* 22 e Å^{-5}). The geometry of the VSCCs at S1 unambiguously confirms its sp^3 hybridization.

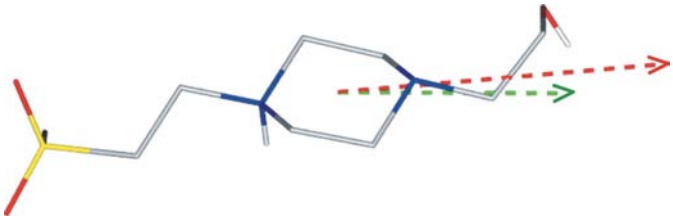

Figure 8
Dipole moment vectors (of arbitrary scale anchored at the center of the six-membered ring), together with the molecule of HEPES. Color coding: green – theoretical model, red – experimental model (from multipole populations).

Table 8
Selected numerical values of hydrogen bonds.

The point $\boldsymbol{r}_{BCP}$ refers to the BCP between the H atom and the acceptor of the hydrogen bond. van der Waals radii were taken from Bondi (1964). Values of G and V were calculated according to the Abramov approximation (Abramov, 1997). Symmetry transformations are the same as in Fig. 9.

	Hydrogen bond	
Parameter	N1—H1···O1^{i}	O4—H2···N2^{ii}
Mutual penetration: Δr_H (Å)	0.44	0.45
Δr_A (Å)	0.41	0.32
$\rho(\boldsymbol{r}_{BCP})$ (e Å^{-3})	0.36 (4)	0.30 (4)
$L(\boldsymbol{r}_{BCP})$ (e Å^{-5})	−1.77 (8)	−0.62 (8)
$G(\boldsymbol{r}_{BCP})$ (a.u.)	0.009	0.012
$V(\boldsymbol{r}_{BCP})$ (a.u.)	−0.036	−0.030
$E(\boldsymbol{r}_{BCP})$ (a.u.)	−0.027	−0.018

3.2.4. Intermolecular hydrogen bonds.. A summary of selected numerical parameters describing the N···H···O hydrogen bonds according to the Koch and Popelier criteria (Koch & Popelier, 1995) is presented in Table 8 and the negative Laplacian maps are shown in Fig. 10. For values of the integrated charges, see also Table 6.

In both cases the criteria concerning the existence of a BCP between an H atom and an acceptor, namely the values of $\rho(\boldsymbol{r}_{BCP})$ and $L(\boldsymbol{r}_{BCP})$, and the mutual penetration of weakly interacting atoms, are fulfilled. $\Delta r_H + \Delta r_A > 0$ and $\Delta r_H - \Delta r_A > 0$, which indicates that atoms mutually penetrate each other and H atoms are clearly donors. The electron density and negative Laplacian are close to the ranges proposed by Koch and Popelier. In Fig. 10 the negative Laplacian maps show that both interactions can be referred to as closed-shell electrostatic ones [*e.g.* the value of $L(\boldsymbol{r}_{BCP})$ is negative]. In the case of the O—H···N bond, a significant polarization of the N atom's

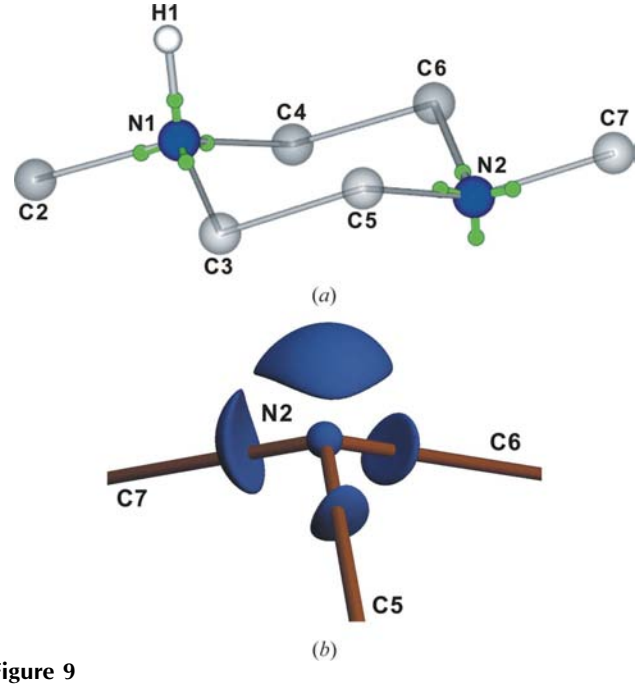

Figure 9
(*a*) Orientation of the VSCCs (small green spheres) around N1 and N2 atoms; (*b*) isosurface plot of $L(\boldsymbol{r})$ at the 45 e Å^{-5} level around the N2 atom.

lone electron pair (non-bonding VSCC) towards the donor hydrogen is observed, while the O atom is much more spherical. Interestingly, a strong polarization of the H atoms in the hydrogen bonds can be observed. A similar effect was observed by Overgaard and co-workers (Overgaard *et al.*, 2001) as well as by Roversi & Destro (2004). Such subtle effects seem to be modeled properly by introducing, at least, quadrupolar terms at the H atoms.

For the N1—H1···O1 intermolecular hydrogen bond, the AIM charges show that both heavy atoms (nitrogen and oxygen) are negatively charged, while the H atom has a positive charge. This is in in accordance with our expectations, as both N and O atoms are bound only to the elements exhibiting lower electronegativity. The O atom is much more negative than nitrogen, which is due to the nature of the whole sulfonic group. The nitrogen is bound to three C atoms, and its charge is lower than that for nitrogen in Schiff bases (C═N—*R* fragment), for example. A similar result is obtained for the O4—H2···N2 hydrogen bond. The O atom from the hydroxyl group is less negative than the respective one from SO_3. Also the H2 atom is slightly more positively charged than H1. The proportional relationship between hydrogen-bond energy and potential energy density, as proposed by Espinosa and co-workers (Espinosa *et al.*, 1998), suggested that the N—H···O bond is stronger than the O—H···N bond. This could be due to an additional stabilization resulting from an extra polarization effect appearing in the ionic hydrogen bonds. One would expect that the N2 atom may be protonated more readily due to the electron-withdrawing effect of the sulfonic group, yet this form is not observed in the solid state.

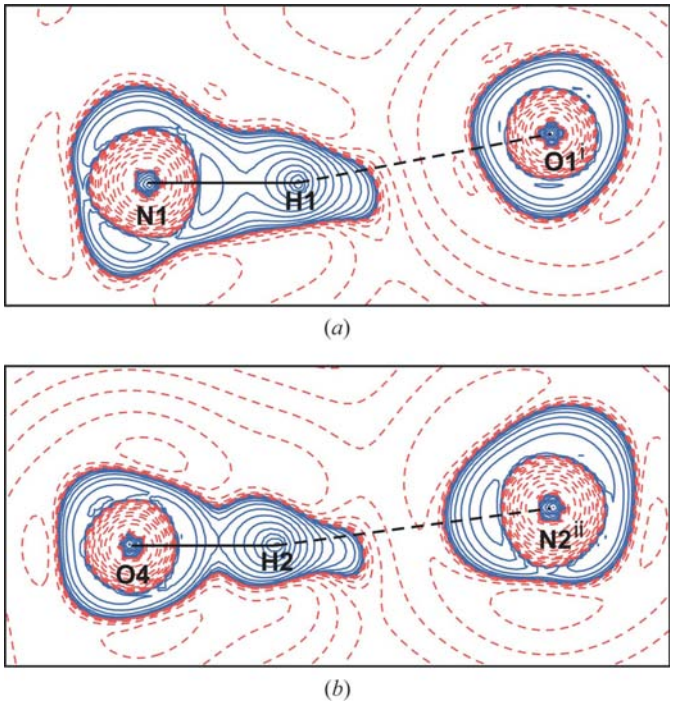

Figure 10
Negative Laplacian maps for: (*a*) N1—H1···O1^{i} [(i) $x+\frac{1}{2}, -y+\frac{1}{2}, -z+2$; N1H1O1^{i} plane] and (*b*) O4—H2···N2^{ii} [(ii) $x+\frac{1}{2}, y, -z+\frac{3}{2}$; O4H2N2^{ii} plane] hydrogen bonds, obtained from experimental charge density. Blue solid lines denote positive values and red dashed lines negative ones. Contours at $\pm$ 0.001 $\times$ 2^n e Å^{-5} (n = 0, 1, 2, ...).

4. Conclusions

A full structural analysis of HEPES has been undertaken in order to understand the relationships between its buffering capacity, structure, ability to form intermolecular interactions and the parallels between its properties in solution and in the crystal.

The Hansen–Coppens formalism, followed by QTAIM, was successfully applied to study charge densities in an organic molecule containing sulfur as the heaviest atom. Our charge density results agree well with those previously obtained for taurine. Experimental data reproduces the molecular properties well (for example, the dipole moment). Additionally, on the basis of the Koch and Popelier criteria and the Espinosa suggestion, it is possible to differentiate hydrogen bonds. It appears that the N—H···O interaction is slightly stronger than the O—H···N interaction. The protonation mode observed in the crystal structure is different from that expected in solution.

The X-ray single-crystal measurement was performed at the Structural Research Laboratory (Department of Chemistry, Warsaw University, Poland), established with financial support from the European Regional Development Found in the Sectoral Operational Programme 'Improvement of the Competitiveness of Enterprises, years 2004–2006' project no WKP_1/1.4.3./1/2004/72/72/165/2005/U. KW thanks the Ministry of Science and Higher Education for financial support – grant 1 T09A 116 30 and the Foundation for Polish Science for financial support within the 'Mistrz' programme. The authors gratefully acknowledge the Interdisciplinary Centre for Mathematical and Computational Modelling in Warsaw (grant No. G33-14) for providing computer facilities. RK would like to thank also Professor Mark Spackman (University of Western Australia) and Dr Parthapratim Munshi (Nancy University) for their help in estimation of the dipole moment and providing the program *LORENTZ*. RK and PŚ would like to thank Polish Ministry of Science and Higher Education for studentships.

References

Abramov, Yu. A. (1997). *Acta Cryst.* A**53**, 264–272.
Allen, F. H., Kennard, O., Watson, D. G., Brammer, L., Orpen, A. G. & Taylor, R. (1987). *J. Chem. Soc. Perkin Trans. II*, pp. S1–S19.
Bader, R. F. W. (1990). *Atoms in Molecules – A Quantum Theory*. Oxford University Press.
Bąk, J. M., Dominiak, P. M., Wilson, C. C. & Woźniak, K. (2009). *Acta Cryst.* A**65**, 490–500.
Becke, A. D. (1993). *J. Chem. Phys.* **98**, 5648–5652.
Blessing, R. H. (1987). *Cryst. Rev.* **1**, 3–58.
Blessing, R. H. (1989). *J. Appl. Cryst.* **22**, 396–397.
Blessing, R. H. (1995). *Acta Cryst.* A**51**, 33–38.
Bondi, A. (1964). *J. Phys. Chem.* **68**, 441–451.
Bruker AXS (2008). *SAINT*, Version 7.60A. Bruker AXS Inc., Madison, Wisconsin, USA.

Chruszcz, M., Zheng, H., Cymborowski, M., Gawlicka-Chruszcz, A. & Minor, W. (2005). *Acta Cryst.* E**61**, o3190–o3191.
Dominiak, P. M. & Coppens, P. (2006). *Acta Cryst.* A**62**, 224–227.
Dominiak, P. M., Volkov, A., Dominiak, A. P., Jarzembska, K. N. & Coppens, P. (2009). *Acta Cryst.* D**65**, 485–499.
Drašković, B. M., Bogdanović, G. A., Neelakantan, M. A., Chamayou, A.-C., Thalamuthu, S., Avadhut, Y. S., auf der Günne, J. S., Banerjee, S. & Janiak C. (2010). *Cryst. Growth Des.* **10**, 1665–1676.
Espinosa, E., Molins, E. & Lecomte, C. (1998). *Chem. Phys. Lett.* **285**, 170–173.
Fournier, B., Bendeif, E.-E., Guillot, B., Podjarny, A., Lecomte, C. & Jelsch, C. (2009). *J. Am. Chem. Soc.* **131**, 10929–10941.
Frisch, M. J. *et al.* (2004). *GAUSSIAN*03, Revision E.01. Gaussian Inc., Wallingford CT, USA.
Gao, F., Yin, C., Yang, P. & Xue, G. (2004). *Acta Cryst.* E**60**, o1328–o1329.
Good, N. E., Winget, G. D., Winter, W., Connoly, T. N., Izawa, S. & Singh, R. M. M. (1966). *Biochemistry*, **5**, 467–477.
Hansen, N. K. & Coppens, P. (1978). *Acta Cryst.* A**34**, 909–921.
Hibbs, D. E., Austin-Woods, C. J., Platts, J. A., Overgaard, J. & Turner, P. (2003). *Chem. Eur. J.* **9**, 1075–1084.
Hirshfeld, F. L. (1976). *Acta Cryst.* A**32**, 239–244.
Hoser, A. A., Dominiak, P. M. & Woźniak, K. (2009). *Acta Cryst.* A**65**, 300–311.
International Tables for Crystallography (2006). 1st online ed. Chester: International Union of Crystallography. [doi:10.1107/97809553602060000001]
Koch, U. & Popelier, P. L. A. (1995). *J. Phys. Chem.* **99**, 9747–9754.
Kubicki, M., Adamiak, D. A., Rypniewski, W. R. & Olejniczak, A. (2007). *Acta Cryst.* E**63**, o2604–o2606.
Lee, C., Yang, W. & Parr, R. G. (1988). *Phys. Rev. B*, **37**, 785–789.
Madsen, A. Ø. (2006). *J. Appl. Cryst.* **39**, 757–758.
Overgaard, J., Schiøtt, B., Larsen, F. K. & Iversen, B. B. (2001). *Chem. Eur. J.* **7**, 3756–3767.
Petersson, G. A., Bennett, A., Tensfeldt, T. G., Al-Laham, M. A., Shirley, W. A. & Mantzaris, J. (1988). *J. Chem. Phys.* **89**, 2193–2218.
Roversi, P. & Destro, R. (2004). *Chem. Phys. Lett.* **386**, 472–478.
Sheldrick, G. M. (2008). *Acta Cryst.* A**64**, 112–122.
Spackman, M. A. (1992). *Chem. Rev.* **92**, 1769–1797.
Spackman, M. A. & Byrom, P. G. (1997). *Chem. Phys. Lett.* **267**, 215–220.
Spackman, M. A. & Jayatilaka, D. (2009). *CrystEngComm*, **11**, 19–32.
Spackman, M. A., Munshi, P. & Jayatilaka, D. (2007). *Chem. Phys. Lett.* **443**, 87–91.
Su, Z. & Coppens, P. (1998). *Acta Cryst.* A**54**, 646–652.
Śledź, P., Minor, T. & Chruszcz, M. (2009). *Acta Cryst.* E**65**, o3027–o3028.
Volkov, A., Macchi, P., Farrugia, L. J., Gatti, C., Mallinson, P., Richter, T. & Koritsanszky, T. (2006). *XD*2006. University at Buffalo, State University of New York, NY, USA.
Woon, D. E. & Dunning, T. H. (1993). *J. Chem. Phys.* **98**, 1358–1371.
Wouters, J., Häming, L. & Sheldrick, G. (1996). *Acta Cryst.* C**52**, 1687–1688.
Wouters, J. & Stalke, D. (1996). *Acta Cryst.* C**52**, 1684–1686.